Electronic Supplementary Material (ESI) for Catalysis Science & Technology.

Supporting Information

CoP nanorods anchored on Ni_2P-NiCoP nanosheets with abundant heterogeneous interfaces boosting the electrocatalytic oxidation of 5-hydroxymethyl-furfural

Mingjun Zhou,[a] Jianmin Chen,[a]* Yingwei Li[a,b]*

[a] *School of Chemistry and Chemical Engineering, South China University of Technology, Guangzhou 510640, China*

[b] *South China University of Technology−Zhuhai Institute of Modern Industrial Innovation, Zhuhai 519175, China*

*Corresponding author. E-mail: chenjianmin@scut.edu.cn; liyw@scut.edu.cn

Contents

Experimental section

Chemicals. All chemicals were purchased from commercial sources and used without further treatment. Nickel acetate tetrahydrate ($Ni(CH_3COO)_2·4H_2O$, AR), cobalt(II) acetate tetrahydrate ($Co(CH_3COO)_2·4H_2O$, AR), cobalt nitrate hexahydrate ($Co(NO_3)_2·6H_2O$, AR), terephthalic acid (BDC, AR), 2-methylimidazole (2-MeIM, AR), hexadecyltrimethylammonium bromide (CTAB, AR), N,N-dimethylacetamide (DMA, $CH_3C(O)N(CH_3)_2$, AR), potassium hydroxide (KOH, 95%), sodium hypophosphite monohydrate ($NaH_2PO_2·H_2O$, AR), Nafion (5 wt%, Hesen), 5-hydroxymethylfurfural (HMF, 99%), 2,5-furandicarboxylic acid (FDCA, 98%), 2,5-diformylfuran (DFF, 98%), 5-formyl-2-furancarboxylic acid (FFCA, 98%) and 5-hydroxymethyl-2-furancarboxylic acid (HMFCA, 98%) were purchased from Aladdin Chemical Co. Ltd. Absolute ethanol (CH_3CH_2OH, AR) and absolute methanol (CH_3OH, AR) were obtained from Guangdong Guanghua Sci-Tech Co. Ltd.

Preparation of Ni-BDC. Typically, 1.5 mmol $Ni(CH_3COO)_2·4H_2O$ was dissolved into 90 mL DI water and stirred for 0.5 h. 0.75 mmol terephthalic acid was dissolved into 90 mL DMA and stirred for 0.5 h. Subsequently, the terephthalic acid solution was added to the nickel acetate solution rapidly with vigorous stirring. After stirring for 0.5 h, the mixture solution was transferred into a Teflon-lined stainless-steel autoclave. The autoclave was sealed and heated at 150 ^oC for 3 h. After cooling to room temperature, the resulting solid product was separated via centrifugation and washed several times with DMA and ethanol.

Preparation of NiCo-BDC. The synthesis of NiCo-BDC was similar to the procedure of Ni-BDC except for using 0.75 mmol $Co(CH_3COO)_2·4H_2O$ and 0.75mmol $Ni(CH_3COO)_2·4H_2O$ as the starting material.

Preparation of NiCo-BDC@ZIF-67. 45 mg Ni-BDC, 6 mg CTAB, 0.6 mmol $Co(NO_3)_2·6H_2O$ and 15 mL DI water were mixed under ultrasonic condition for 10 min and stirred for 2h. Besides, 4.8 mmol 2-MeIM was dissolved into 15 mL DI water.

Then, the 2-MeIM solution was added dropwise into the above mixture solution and stirred for 2 h. The resultant purple solid was collected by centrifugation and washed with absolute methanol for several times. After drying in an oven overnight at 60 ^oC, the NiCo-BDC@ZIF-67 was obtained.

Preparation of rod-like ZIF-67. 6 mg CTAB, 0.6 mmol $Co(NO_3)_2{\cdot}6H_2O$ and 15 mL DI water were mixed under ultrasonic condition for 10 min and stirred for 2h. Besides, 4.8 mmol 2-MeIM was dissolved into 15 mL DI water. Then, the 2-MeIM solution was added dropwise into the above mixture solution and stirred for 2 h. The resultant purple solid was collected by centrifugation and washed with absolute methanol for several times. After drying in an oven overnight at 60 ^oC, the rod-like ZIF-67 was obtained.

Preparation of Co/Ni-NiCo@NC-T. In a typical synthesis, NiCo-BDC@ZIF-67 was placed in a tube furnace, heated to 600 ^oC at a ramp rate of 2 ^oC min^{-1} and kept for 3 h under flowing Ar atmosphere. A series of samples with different carbonization temperatures were prepared. The products were named as Co/Ni-NiCo@NC-T (T = 500, 600, 700 and 800 ^oC), where T represents the carbonization temperature.

Preparation of CoP/Ni_2P-NiCoP@NC-T. 20 mg of the as-obtained Co/Ni-NiCo@NC-T was placed in the middle of the tubular furnace, while $NaH_2PO_2{\cdot}H_2O$ (400 mg) was placed on its upstream side. Then, the samples were heated to 300 ^oC for 2 h at a heating rate of 2 $^oC{\cdot}min^{-1}$ under Ar atmosphere.

Preparation of Ni_2P@C, CoP@NC and CoP-Ni_2P-NiCoP@C. The synthesis of Ni_2P@C, CoP@NC and CoP-Ni_2P-NiCoP@C was similar to the preparation of CoP/Ni_2P-NiCoP@NC-600 except that Ni-BDC, rod-like ZIF-67, NiCo-BDC were used as the precursor, respectively.

Preparation of Ni_2P@C-CoP@NC. The physical mixture Ni_2P@C-CoP@NC was prepared by mixing the Ni_2P@C and CoP@NC based on their element contents in order to make sure that the contents of Ni and Co are the same as CoP/Ni_2P-NiCoP@NC-

600. Based on the results of element analysis for Ni_2P@C and CoP@NC, about 0.7 mg Ni_2P and 1.1 mg CoP@NC were used.

Characterizations. X-ray diffraction (XRD) patterns of the samples were collected on a Bruker D8 ADVANCE with a Rigaku diffractometer (D/MAX/IIIA, 3 kW), using Cu Kα radiation (40 kV, 40 mA, λ= 0.1543 nm). Raman spectra were recorded on a LabRAM Aramis Raman Spectrometer (HORIBA Jobin Yvon). The metal contents in the samples were measured quantitatively by Atomic Absorption Spectroscopy (AAS, HITACHI Z-2300 instrument). Fourier transform infrared spectroscopy (FTIR) spectra of all samples in KBr pellet were recorded on a Bruker Vector33 spectrometer. Thermogravimetric analysis (TGA) was performed on a NETZSCH STA 449F3 heating from 30 to 800 ^{o}C in nitrogen atmosphere at a ramping rate of 10 ^{o}C min^{-1}. BET surface areas and pore structure of the samples were measured by N_2 adsorption/desorption isotherms obtained on a Micromeritics ASAP 2020 M instrument at 77 K. All the samples were degassed at 120 ^{o}C for 2 h before the measurement. X-ray photoelectron spectroscopy (XPS) was recorded by using Thermo Scientific K-Alpha+ system with a base pressure of 5×10^{-9} Torr. The surface morphology of the samples was investigated using a high-resolution scanning electron microscopy (SEM, MERLIN of ZEISS). The structure and element mapping were determined by a high-resolution transmission electron microscope (TEM, JEOL, JEM-2100F) with EDX analysis (Bruker Xflash 5030T) operated at 200 kV. The organics were quantified by high-performance liquid chromatography (HPLC, Shimadzu Prominence LC-2030C system) with a refractive index detector.

H_2-TPD experiments. H_2-TPD experiments were performed on an AutoChem II 2920 instrument. 80 mg of sample was heated at 200 °C for 2 h under Ar atmosphere with a flow rate of 50 mL/min in a quartz reactor. When the temperature was cooled to 50 °C, H_2 saturation uptake of the sample was achieved by passing 10% H_2/Ar with a flow rate of 50 mL/min for 60 min. After H_2 adsorption, the sample was purged by Ar for 30 min at a flow rate of 50 mL/min. Then, the sample was heated from 50 to 550 °C at a heating rate of 10 °C/min and maintained at 550 °C for 1 h, while the H_2-TPD profile was recorded with a thermal conductivity detector.

Electrochemical measurements. Electrochemical measurements were performed with a CHI 760E potentiostat (CH Instruments, Inc., Shanghai) supported with the electrochemical station of Pine Instruments (model AFMSRCE) at room temperature. A standard three-electrode system was applied using the platinum wire and the Ag/AgCl (3 M KCl) as the counter and reference electrodes, respectively. The working electrode was prepared according to the following procedures. The catalyst ink was prepared by dispersing 1.8 mg electrocatalyst into 30 μL Nafion, 200 μL deionized water and 200 μL ethanol solution. Then, the catalyst suspension was coated on a piece of clean carbon cloth (1×1 cm) as a working electrode. All of the reported potentials refer to the reversible hydrogen electrode (RHE) scale, which were calculated via the Nernst equation:

$$E_{[RHE]} = E_{[Ag/AgCl]} + 0.197 + 0.059 \times pH \qquad (S1)$$

Catalysts were activated by conducting 40 cyclic voltammetry (CV) cycles between 0.2-0.9 V *vs.* RHE at a scan rate of 50 mV s^{-1}. Then the Linear-sweep voltammetry (LSV) measurements were performed at a scan rate of 5 mV s^{-1} with 90% iR compensation employed in all the electrochemical tests. The electrochemical HMF oxidation tests were conducted in 0.1 M KOH solution with 5 mM HMF. The conversions of electrochemical HMF oxidation were evaluated by chronoamperometry at 1.45 V *vs.* RHE. The CVs were tested to calculated the double-layer capacitance (C_{dl}) with different scan rates of 5, 10, 15, 20 and 25 mV s^{-1} in the potential interval of 0.564 to 0.664 V *vs.* RHE. Electrochemical impedance spectroscopy (EIS) measurements were performed in the frequency ranging from 0.01 to 10^5 Hz with an amplitude of 10 mV.

Production quantification. HPLC (Shimadzu Prominence LC-2030C system) with a refractive index detector was used to analyze the HMF oxidation products. Sulfuric acid (5 mM) was used as the mobile phase in isocratic mode with a flow rate of 1 mL min^{-1}

at 40 °C. Sample aliquots (10 μL) were injected directly into a Shodex SUGARSH-1011 column (8 mm × 300 mm). The identification and quantification of the products were determined from the calibration curves by applying standard solutions with known concentrations. The retention times were 11.4, 14.8, 15.4, 21.5, and 26.2 min for FDCA, HMFCA, FFCA, HMF and DFF, respectively.

The HMF conversion, FDCA yield and Faradaic efficiency were calculated using following equations:

$$\text{HMF conversion (\%)} = \frac{\text{mol of HMF consumed}}{\text{mol of HMF added}} \times 100 \tag{S2}$$

$$\text{FDCA yield (\%)} = \frac{\text{mol of FDCA formed}}{\text{mol of HMF added}} \times 100 \tag{S3}$$

$$\text{Faradaic efficiency (\%)} = \frac{\text{mol of FDCA formed}}{\text{Charge}/(6 \times F)} \times 100 \tag{S4}$$

Where F is the Faradaic constant (96485 C mol^{-1}).

Turnover frequencies (TOFs). The *TOF* value was calculated from the following equation:

$$TOF = \frac{J * A}{6 * F * N} \tag{S5}$$

Where J is the current density obtained at 1.45 V *vs.* RHE and normalized by geometric area; A is the geometric area; F is the Faradaic constant and N is the mole number of active metal atoms on the electrode, calculated via equation (S6).

This method is calculating based on active Ni and Co atoms analyzed by H_2-TPD, from the following equation:

$$N = m \times r \tag{S6}$$

where m is the loading mass of catalysts on carbon cloth, r is the mole of active metal atoms per milligram.

Theoretical calculation. Density functional theory (DFT) calculations were performed using the Vienna Ab initio Simulation Package (VASP) based on the pseudopotential plane wave (PPW) method [S1-3]. The perdew-Bueke-Ernzerhof (PBE) functional was used to describe exchange-correlation effects of electrons [S4]. We have chosen the projected augmented wave (PAW) potentials to describe the ionic cores and take valence electrons into account using a plane wave basis set with a kinetic energy cutoff of 500 eV [S5,6]. In order to simulate the surface structure, (2 1 1) Millar plane of CoP of 4×4×2 supercell was sliced, and an extra vacuum zone of 12 Å was applied along z-direction to avoid interactions between unit cells. The surface models of Ni_2P and NiCoP were built in a similar way with both (1 1 1) plane. Further, a heterojunction model of CoP/Ni_2P-NiCoP was built based on the surface model mentioned above. All structures were first optimized to reach their most stable configuration. During the geometry optimizations, all the atom positions were allowed to relax. In this work, the Brillouin-zone sampling were conducted using Monkhorst-Pack (MP) grids of special points with the separation of 0.04 $Å^{-1}$ [S7]. The convergence criterion for the electronic self-consistent field (SCF) loop was set to 1×10-5 eV/atom. The atomic structures were optimized until the residual forces were below 0.05 $eVÅ^{-1}$.

Gibbs free energy change (ΔG) was evaluated by using the computational hydrogen electrode (CHE) model, which takes one-half of the chemical potential of gaseous hydrogen under standard conditions as the free energy of the proton-electron pairs. ΔG was calculated by the following equation:

$$\Delta G = \Delta E + \Delta E_{ZPE} - T\Delta S + neU \quad \text{(S7)}$$

where ΔE, ΔE_{ZPE}, *and* ΔS are the reaction energy from DFT calculation, the correction of zero-point energy, and the change of simulated entropy, respectively. T is the temperature ($T = 300$ K). n and U are the number of transferred electrons and applied potential, respectively.

Supplementary Figures

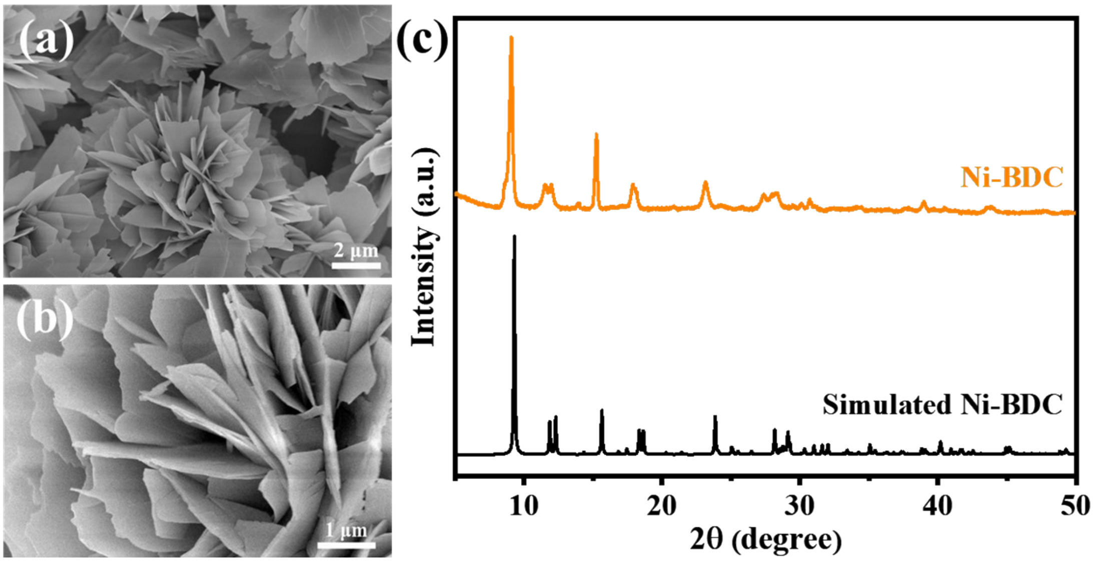

Fig. S1. (a,b) SEM images and (c) XRD patterns of Ni-BDC.

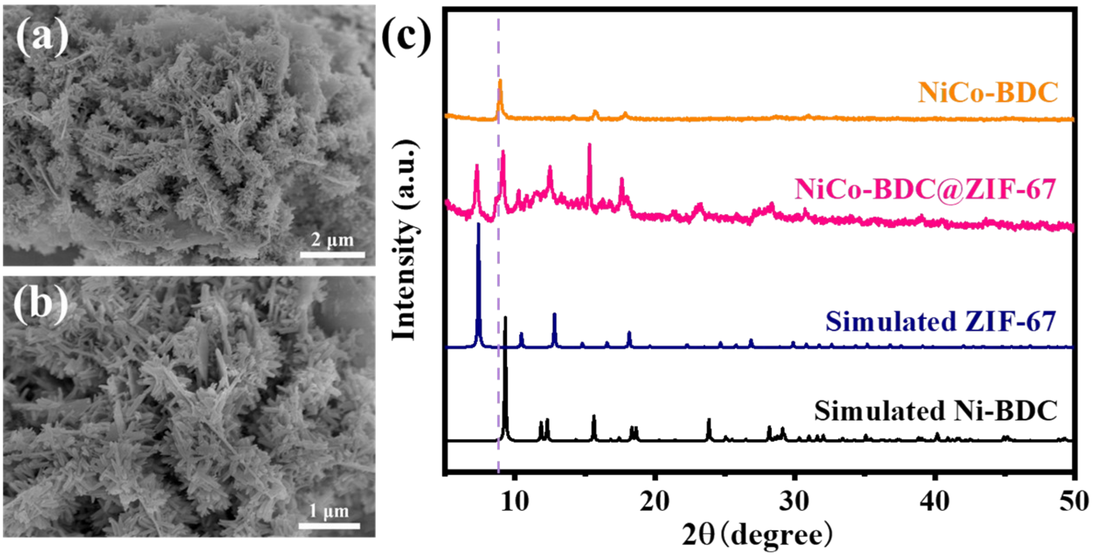

Fig. S2. (a,b) SEM images of NiCo-BDC@ZIF-67 and (c) XRD patterns of NiCo-BDC and NiCo-BDC@ZIF-67.

The X-ray diffraction peaks at 7.4 and 12.8° may be attributed to ZIF-67, while the ones at 9.1, 15.2 and 17.9° are indexed to Ni-BDC (Fig. S2c). Besides, the main diffraction peak around 9.1° of NiCo-BDC@ZIF-67 exhibits a negative shift relative to that of simulated Ni-BDC, which is much closer to that of NiCo-BDC. This indicates that part of Co^{2+} ions replaced the Ni^{2+} in Ni-BDC to form NiCo-BDC during the growth of ZIF-67.

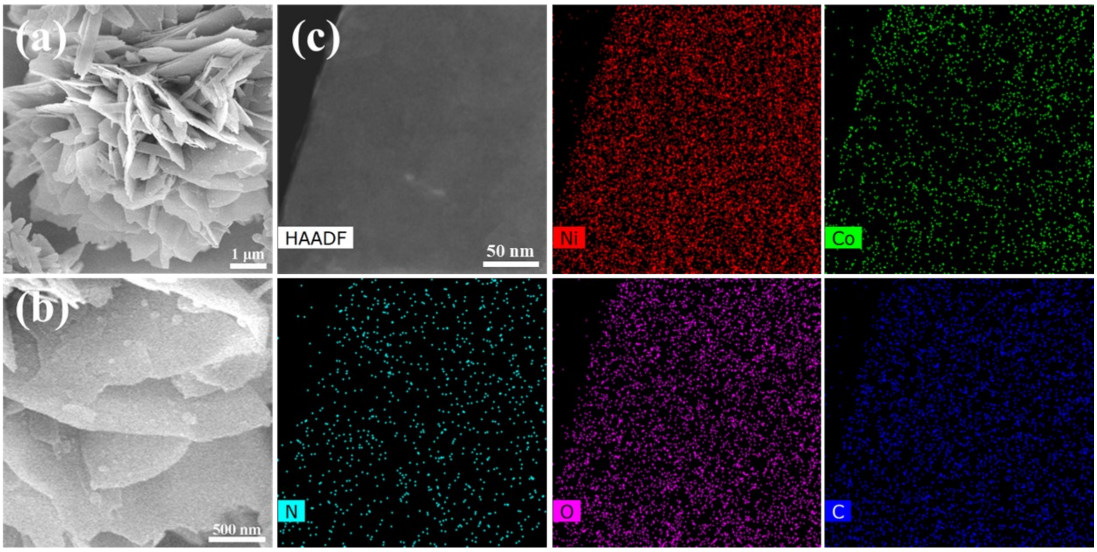

Fig. S3. (a,b) SEM images and (c) HAADF-STEM and corresponding element mapping images of NiCo-BDC where the rod-like ZIF-67 didn't grow on.

As can be seen in Fig. S3c, Ni and Co elements are homogeneously dispersed in the nanosheets, indicating the presence of Co^{2+} and Ni-BDC.

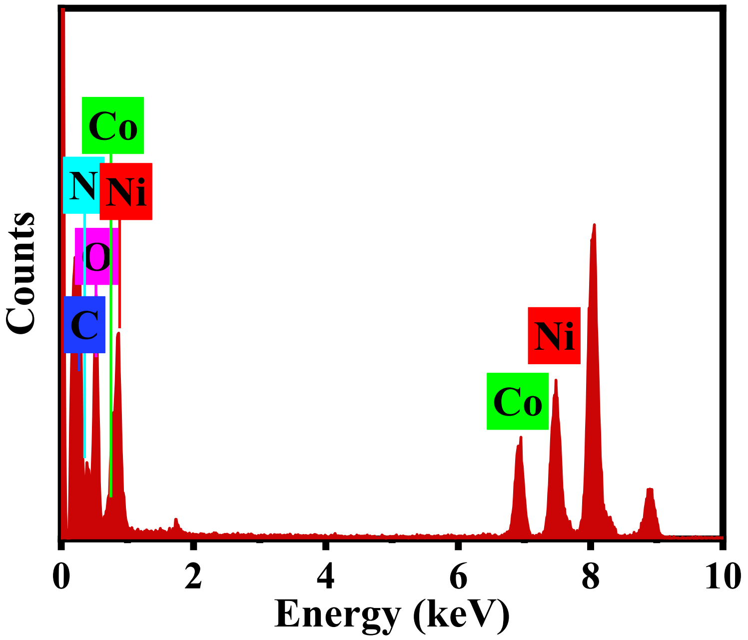

Fig. S4. Energy dispersive X-ray spectroscopy (EDS) spectrum of NiCo-BDC@ZIF-67.

Energy dispersive X ray spectroscopy (EDS) further proves the coexistence of Co, Ni, C, N and O elements.

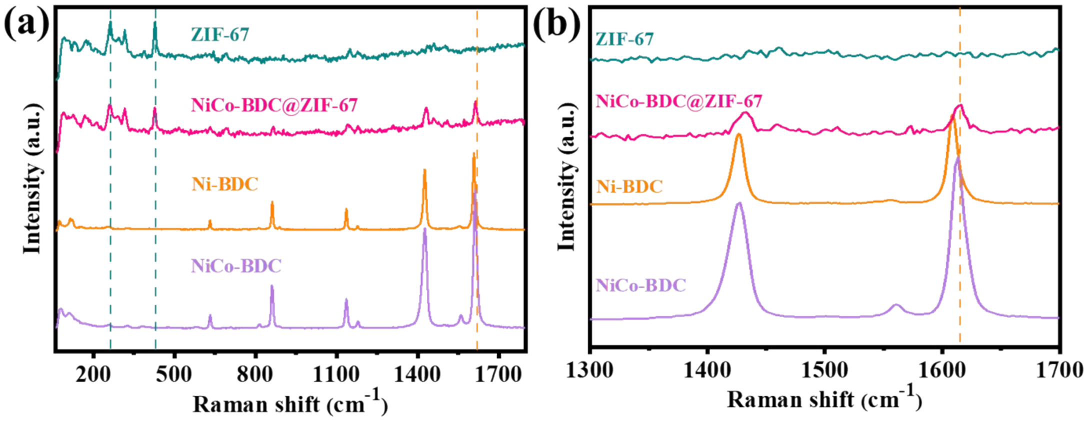

Fig. S5. Raman spectra of ZIF-67, Ni-BDC, NiCo-BDC and NiCo-BDC@ZIF-67.

Raman spectra were carried out to determine the components of NiCo-BDC and ZIF-67. The characteristic peaks at 260.8 and 426.4 cm^{-1} are attributed to ZIF-67, and that at 1614.7 cm^{-1} may be assigned to NiCo-BDC.

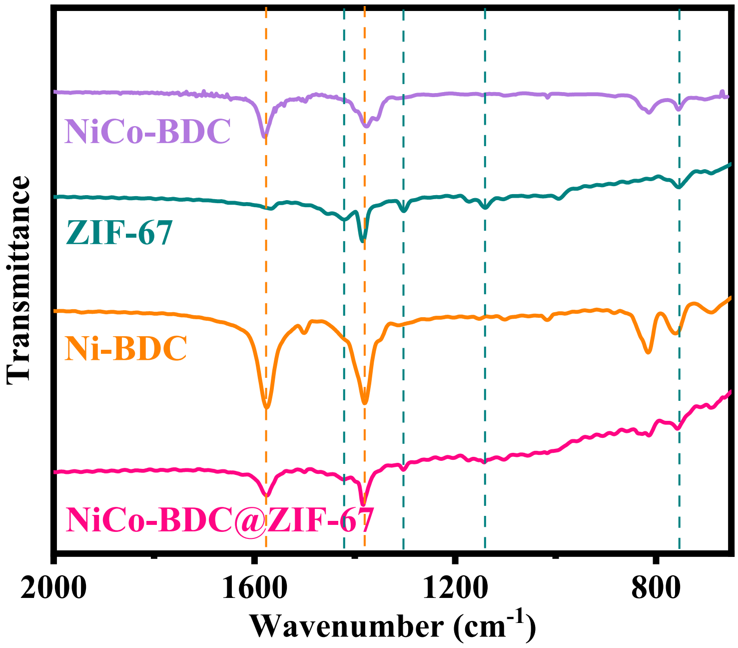

Fig. S6. Fourier transform infrared (FT-IR) spectra of ZIF-67, Ni-BDC, NiCo-BDC and NiCo-BDC@ZIF-67.

To further clarify the components of NiCo-BDC@ZIF-67, the chemical bonds of the components in the samples were investigated by Fourier transform infrared (FT-IR) spectroscopy. The IR bands at 1576 and 1382 cm^{-1} are ascribed to the asymmetric and symmetric vibrations of the COO-, respectively.[S8] Obviously, the typical bands at 1141 cm^{-1}, and 1304 cm^{-1} correspond to the plane vibration of the imidazole ring, and the typical band at 1421 cm^{-1} is assigned to the stretching vibration of the imidazole ring.[S9] The results indicate that ZIF-67 was successfully grown on the nanosheets of Ni-BDC. Besides, the peak at 756 cm^{-1} of NiCo-BDC@ZIF-67 exhibits a negative shift relative to that of Ni-BDC, close to the peak of NiCo-BDC, which further confirms that Ni was partially replaced by Co during the preparation. The combination of the element mapping, Raman and FT-IR results demonstrate that part of the Ni^{2+} ions in the Ni-BDC can be replaced by Co^{2+} to form NiCo-BDC.

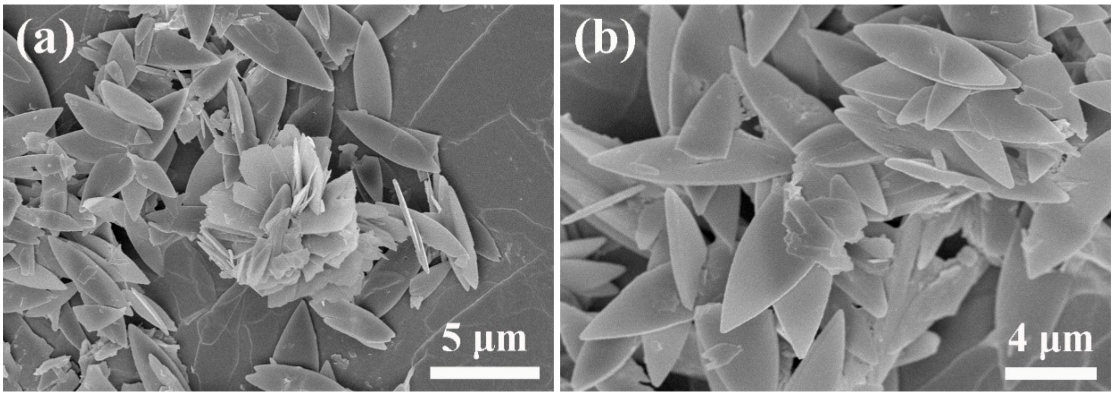

Fig. S7. SEM images of the obtained sample when CTAB was not added in the ZIF-67 growth process.

When CTAB was absent during the growth of ZIF-67, flake-like ZIF-67 was obtained and separated from the Ni-BDC nanosubstrate, suggesting that CTAB was served as an indispensable regulator and anionic adsorbent.

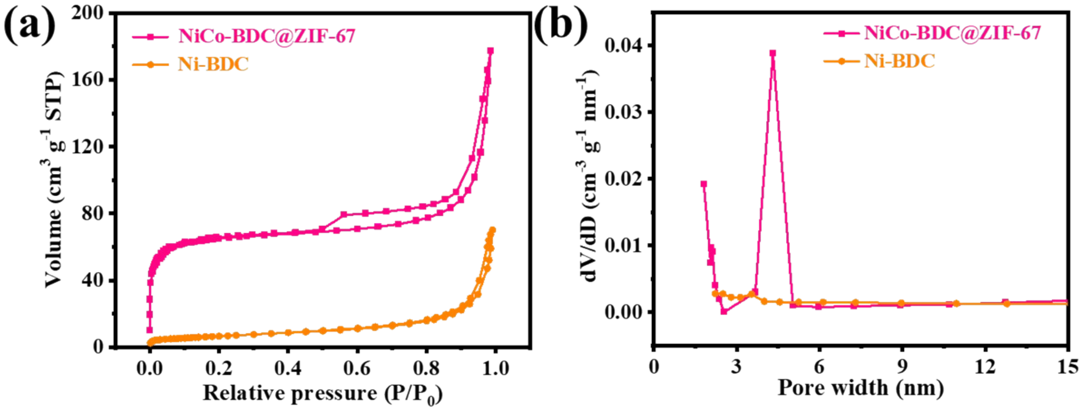

Fig. S8. (a) Nitrogen adsorption-desorption isotherms at 77 K, and (b) the corresponding pore size distribution curves of Ni-BDC and NiCo-BDC@ZIF-67.

The nitrogen adsorption-desorption isotherms of NiCo-BDC@ZIF-67 can be classified as a combined characteristic of type I and IV, in which the pronounced hysteresis loop in the P/P_0 range of about 0.5-1.0 verifies the formation of mesoporous structure. This is probably due to the fact that the 2D Ni-BDC is alkali-etched during the growth of ZIF-67, thus producing coordination defects in the precursor. The Brunauer-Emmett-Teller (BET) surface area of NiCo-BDC@ZIF-67 is measured to be 218 m^2 g^{-1}, which is much larger than that of Ni-BDC (23 m^2 g^{-1}) (Table S1).

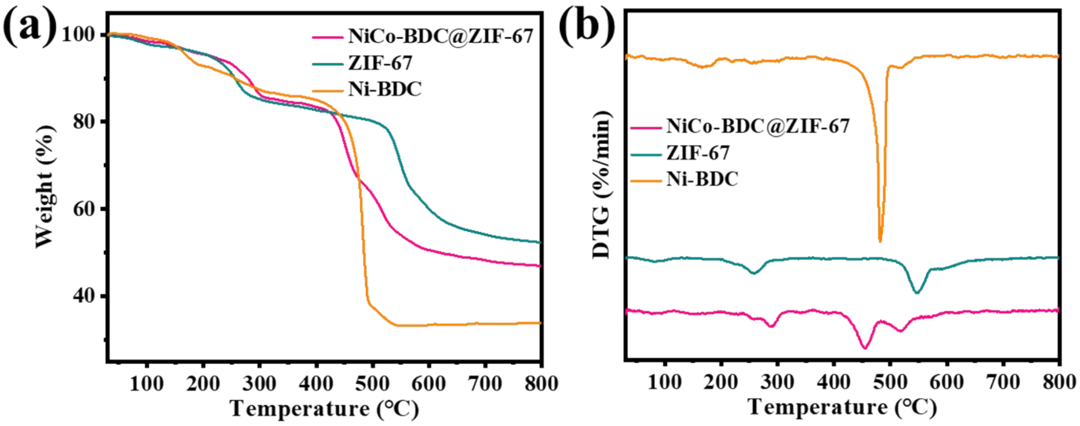

Fig. S9. Thermogravimetric analysis (TGA) for Ni-BDC, ZIF-67 and NiCo-BDC@ZIF-67 in N_2 atmosphere.

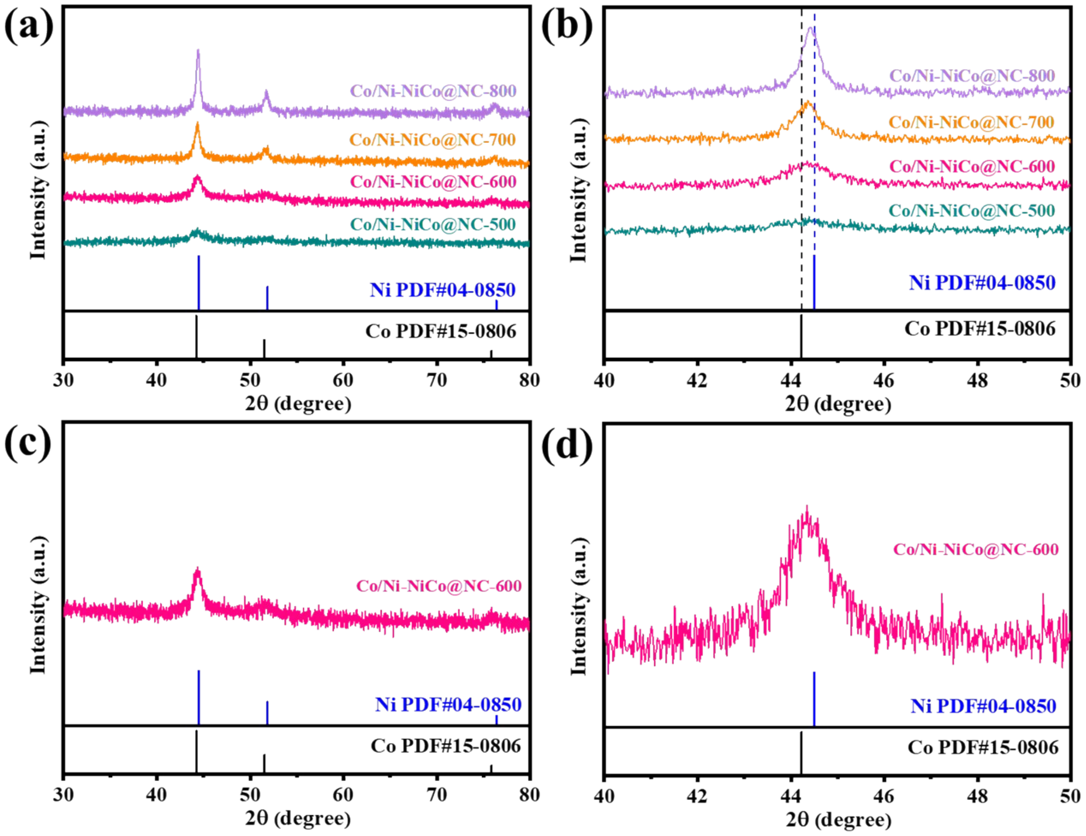

Fig. S10. X-ray diffraction patterns of Co/Ni-NiCo@NC-T (a,b) and Co/Ni-NiCo@NC-600 (c,d).

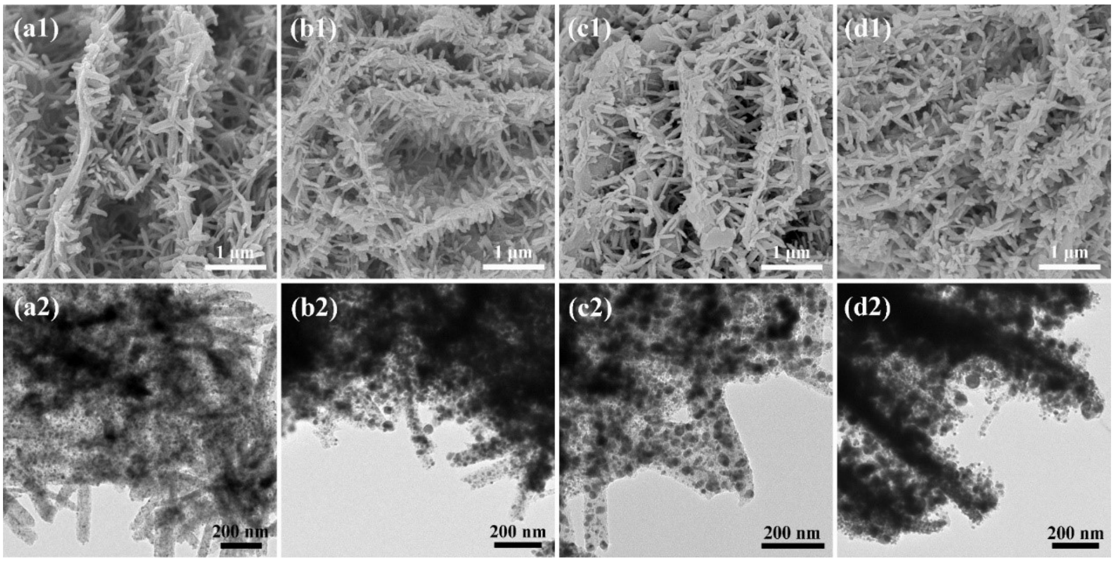

Fig. S11. SEM (a1-d1) and TEM (a2-d2) images of (a1,a2) Co/Ni-NiCo@NC-500, (b1,b2) Co/Ni-NiCo@NC-600, (c1,c2) Co/Ni-NiCo@NC-700 and (d1,d2) Co/Ni-NiCo@NC-800.

As shown in Fig. S11, all the 1D Co@NC-T nanorods with a length of about 200 nm are grown on the surface of 2D Co-Ni-NiCo@NC-T nanosheets with an approximate thickness of 40 nm. In the calcination process, NiCo-BDC in the nanosheets and both ZIF-67 and Ni-BDC on the connecting boundaries are converted into NiCo@NC alloy, while the spatially separated ZIF-67 and Ni-BDC are transformed into Co@NC and Ni@NC, respectively. Therefore, Co/Ni-NiCo@NC-T with a coralline-like morphology could expose abundant active sites, especially on the surface and contact boundaries.

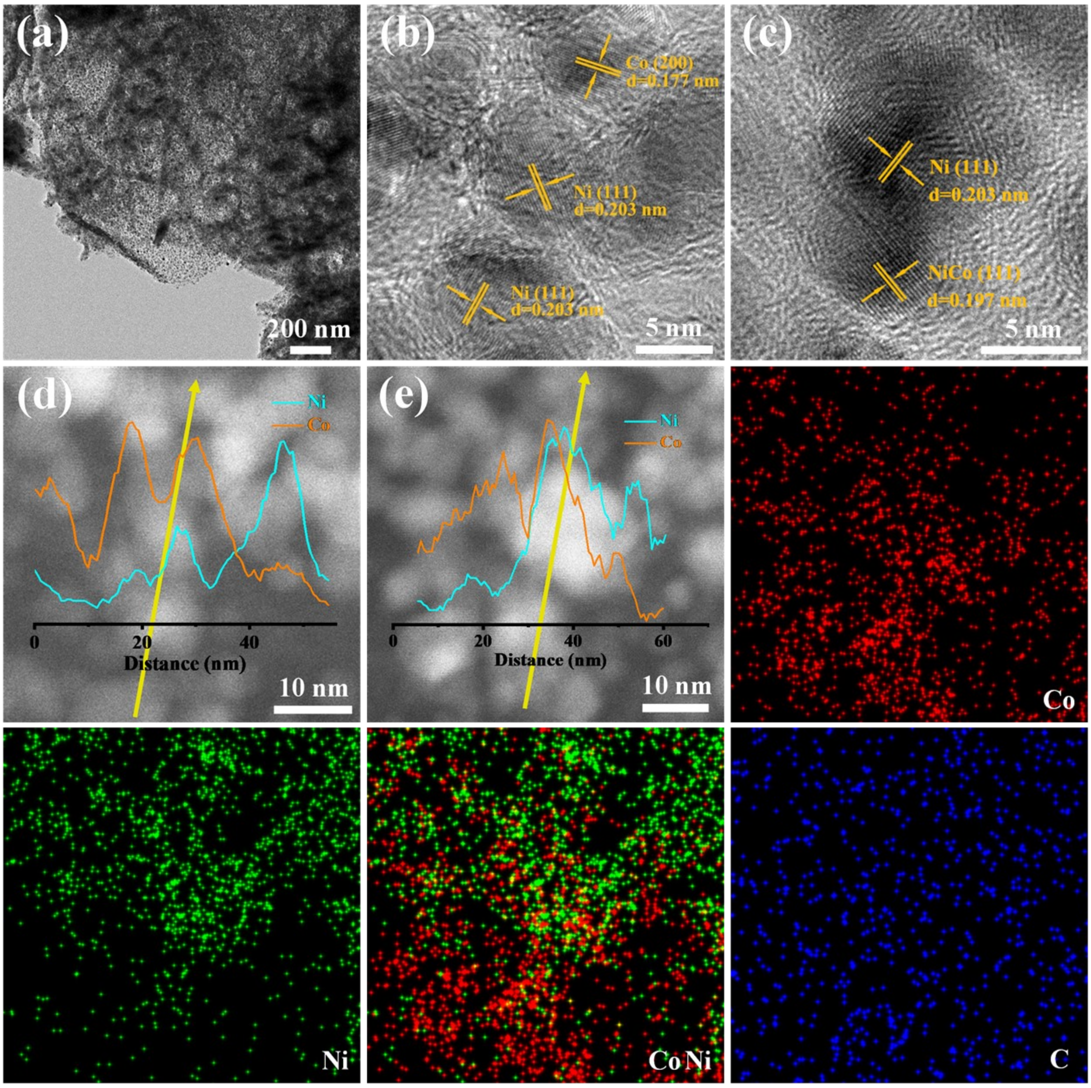

Fig. S12. (a) TEM, (b,c) HR-TEM, and (d,e) HAADF-STEM image, elemental line scan profiles and EDS mapping images of Co/Ni-NiCo@NC-600.

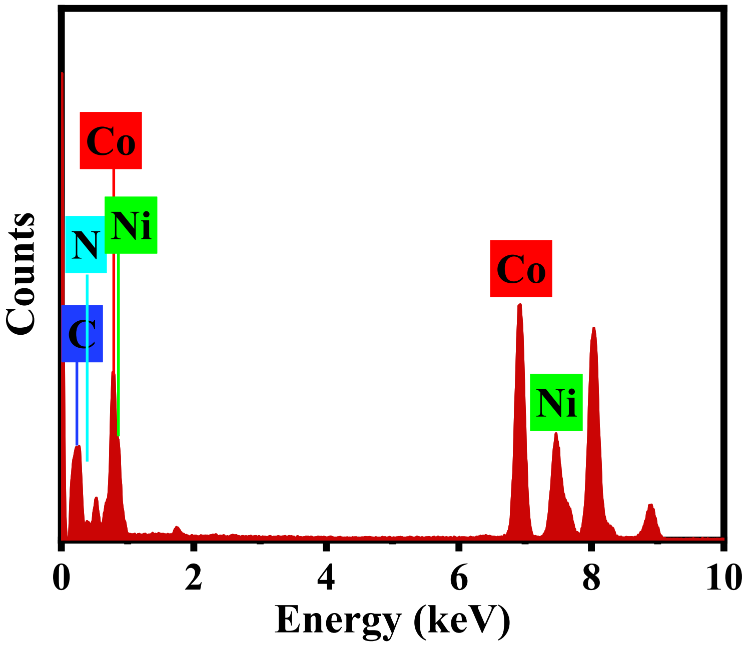

Fig. S13. Energy dispersive X-ray spectroscopy (EDS) spectrum of Co/Ni-NiCo@NC-600.

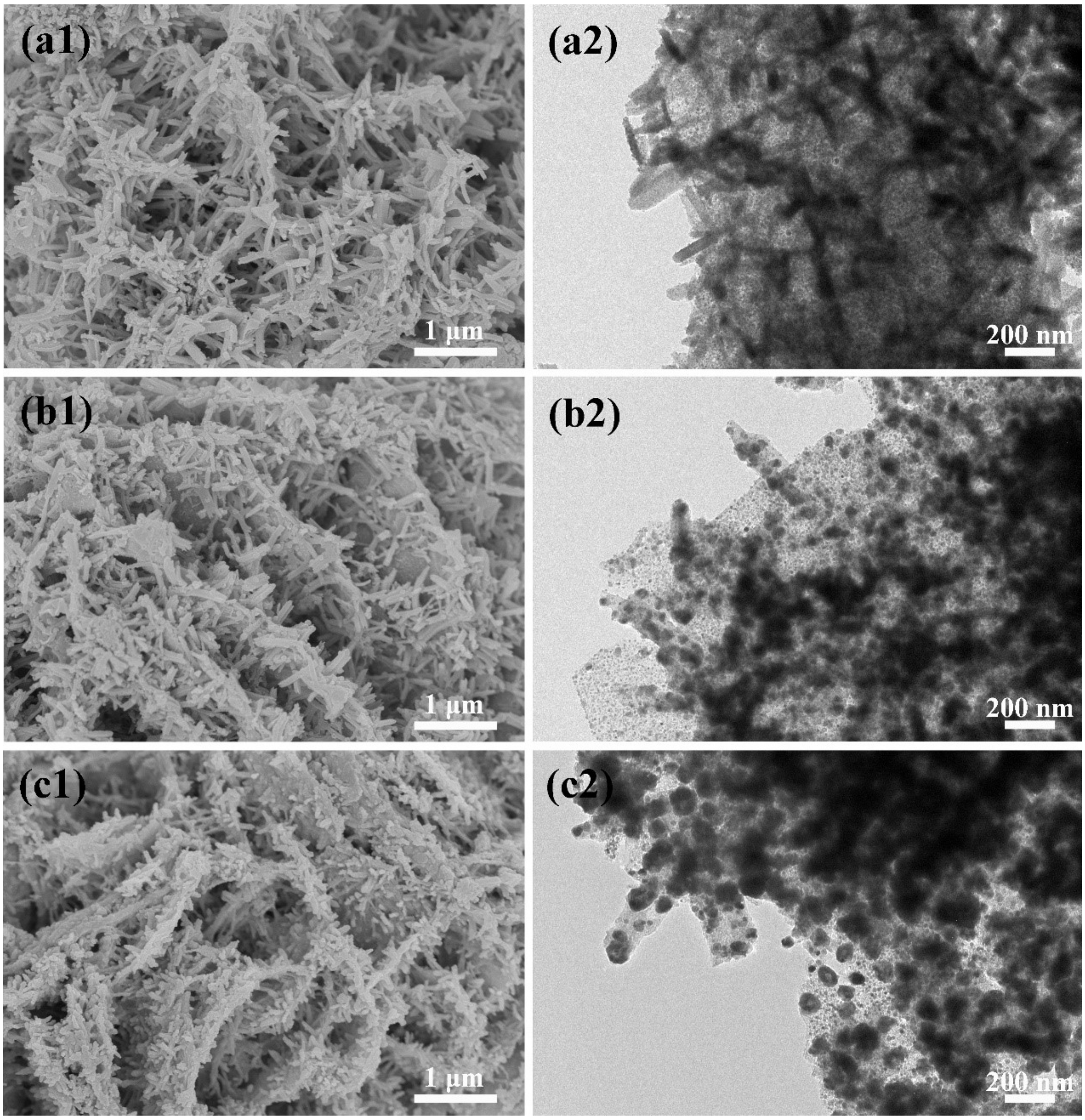

Fig. S14. SEM (a1-c1) and TEM (a2-c2) images of (a1,a2) CoP/Ni_2P-NiCoP@ NC-500, (b1,b2) CoP/Ni_2P-NiCoP@NC-700 and (c1,c2) CoP/Ni_2P-NiCoP@NC-800.

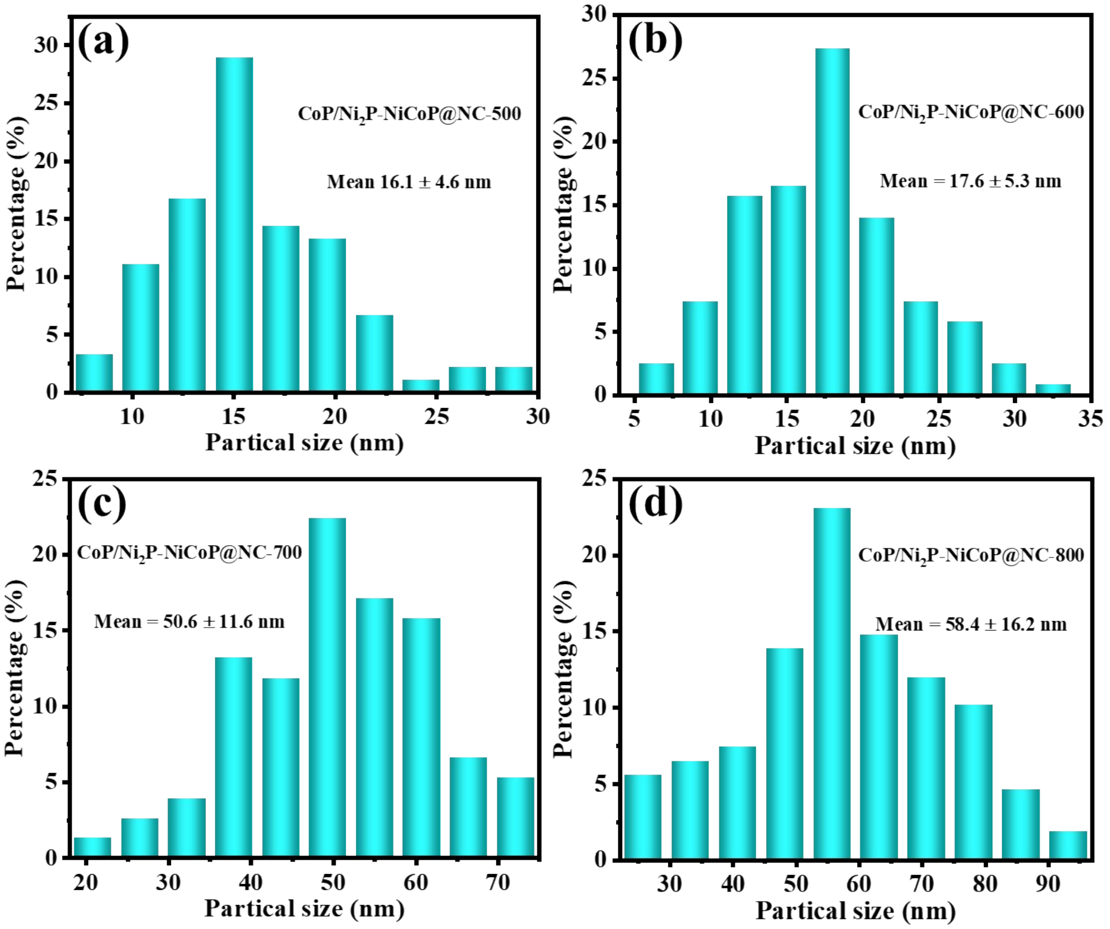

Fig. S15. Particle size distribution of the metal phosphide nanoparticles.

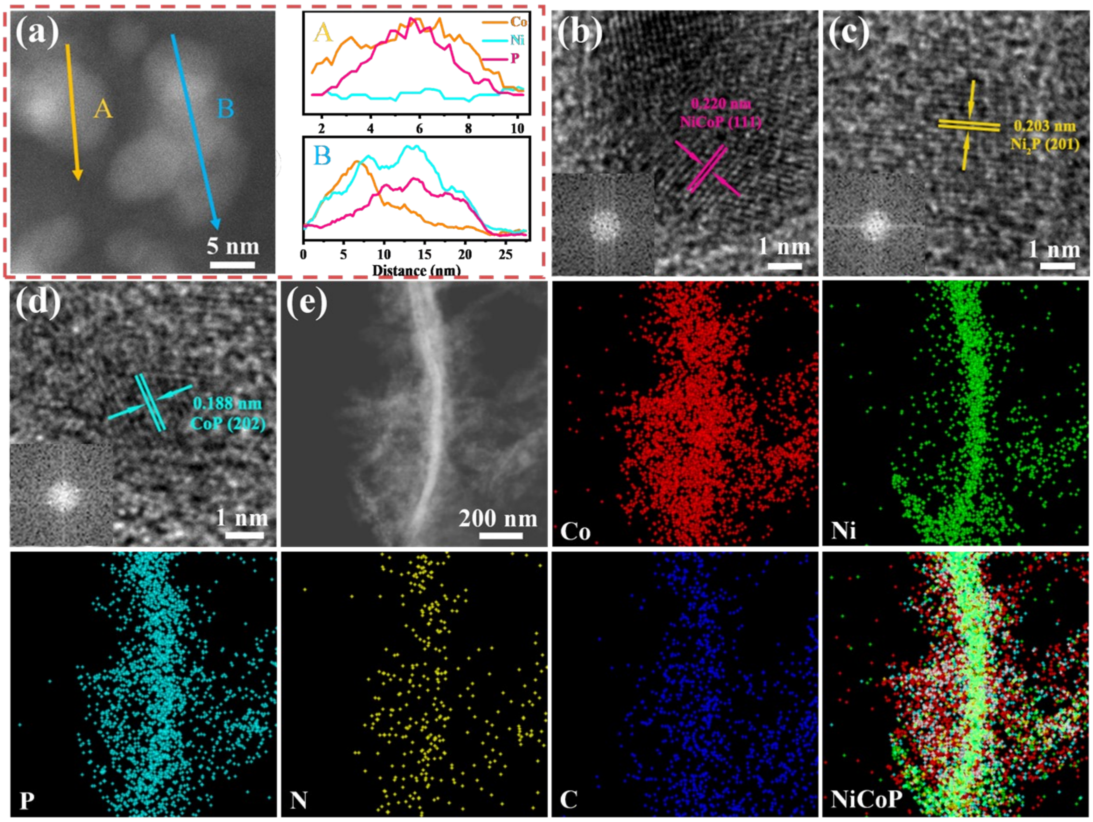

Fig. S16. (a) HAADF-STEM image and elemental line scan profiles, (b-d) HRTEM and fast Fourier transform (FTT) images of a single nanoparticle, (e) HAADF-STEM and EDS mapping images of CoP/Ni_2P-NiCoP@NC-600.

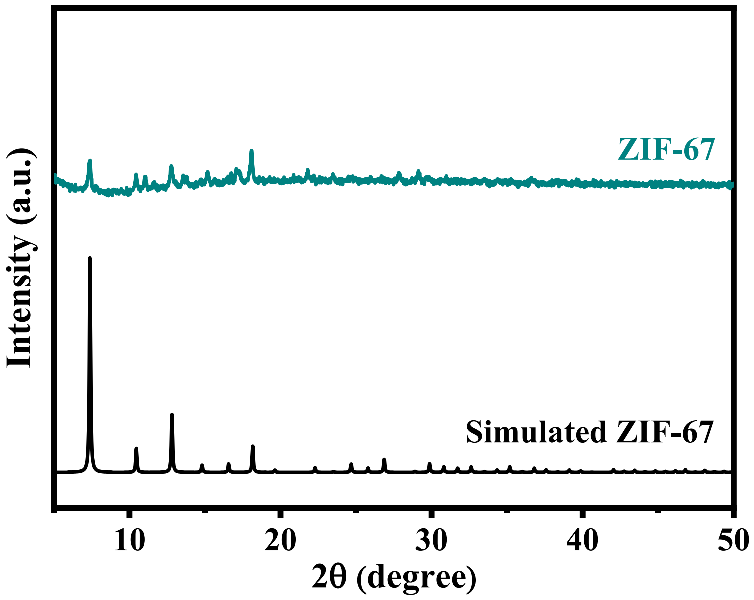

Fig. S17. XRD patterns of rod-like ZIF-67.

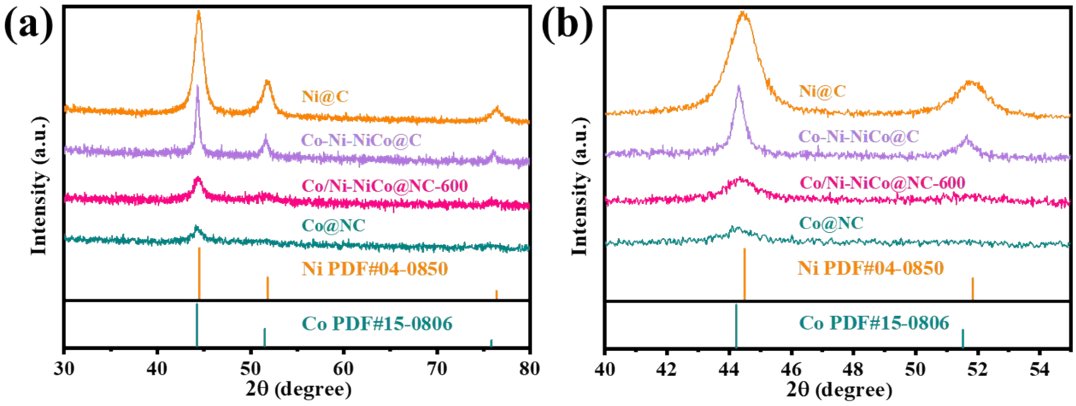

Fig. S18. XRD patterns of Co/Ni-NiCo@NC-600, Ni@C, Co@NC and Co-Ni-NiCo@C.

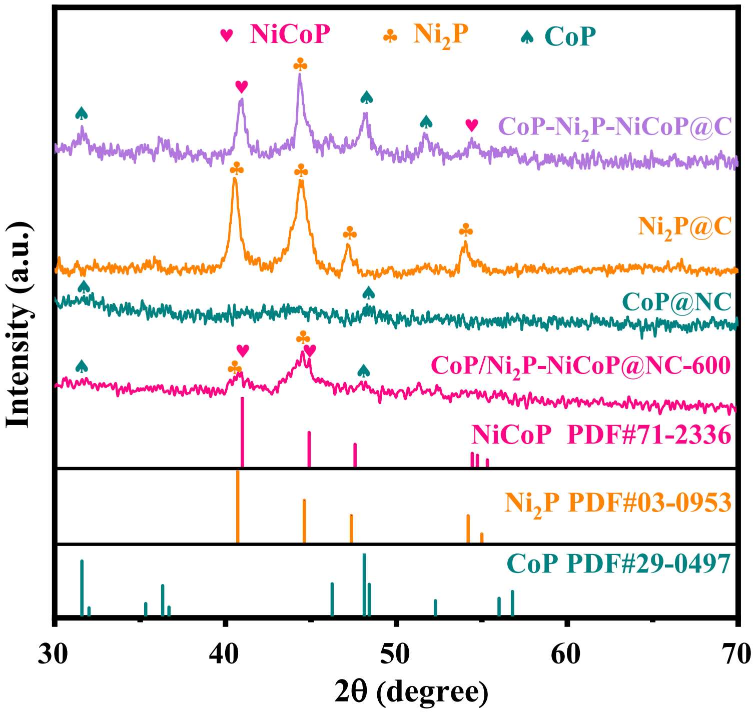

Fig. S19. XRD patterns of CoP/Ni_2P-NiCoP@NC-600, Ni_2P@C, CoP@NC and CoP-Ni_2P-NiCoP@C.

The crystal phase compositions of the CoP/Ni_2P-NiCoP@NC-600 and comparative samples (Ni_2P@C, CoP@NC and CoP-Ni_2P-NiCoP@C) are determined by XRD patterns. The diffraction peaks are corresponding to active species of NiCoP (PDF#71-2336), Ni_2P (PDF#03-0953) and CoP (PDF#29-0497), respectively, indicating the successful synthesis of CoP/Ni_2P-NiCoP@NC-600 hetero-nanostructures. The CoP-Ni_2P-NiCoP@C also possesses these three active species, similar to CoP/Ni_2P-NiCoP@NC-600, which suggests the pure phase NiCoP could not be obtained by using the NiCo-BDC as precursor in this condition. The peaks of Ni_2P@C and CoP@NC are corresponding to Ni_2P (PDF#03-0953) and CoP (PDF#29-0497), respectively.

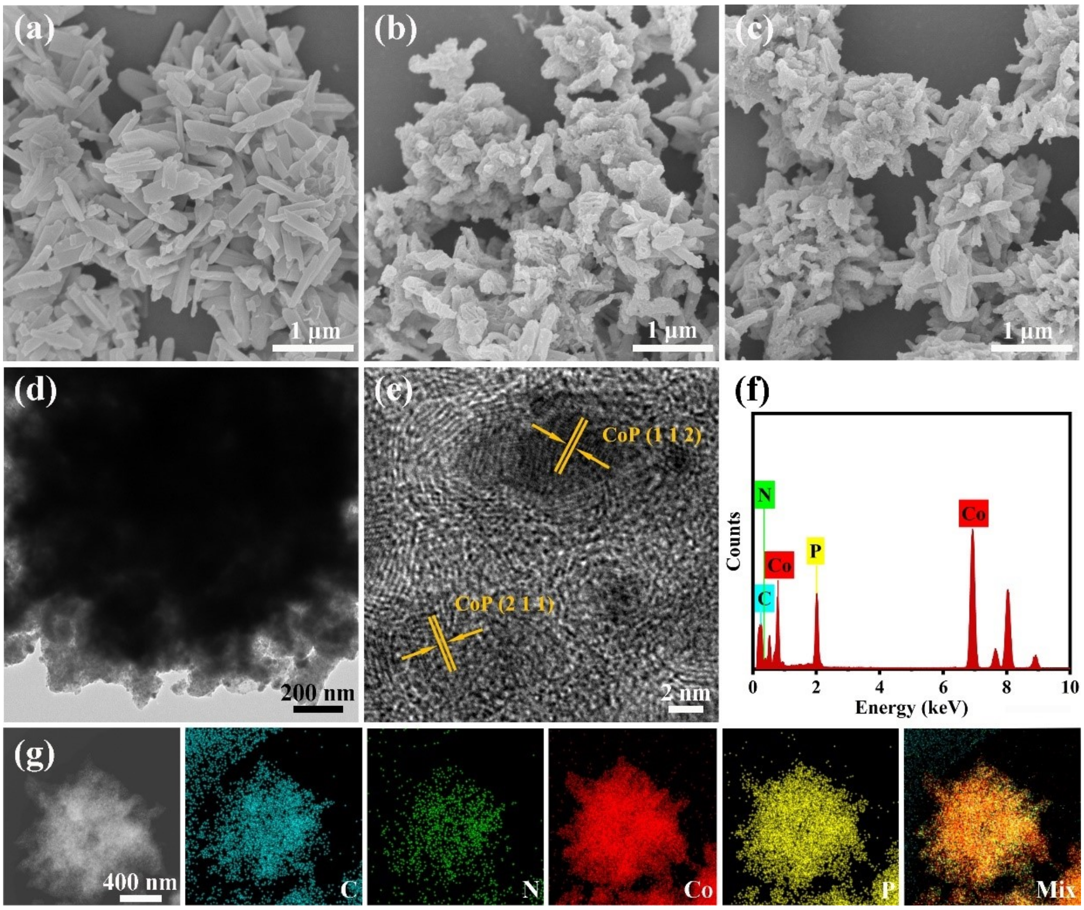

Fig. S20. SEM images of (a) rod-like ZIF-67, (b) Co@NC and (c) CoP@NC. (d) TEM image, (e) HRTEM image, (f) Energy dispersive X-ray spectroscopy (EDS) spectrum, and (g) HAADF-STEM and EDS mapping images of CoP@NC.

In order to make a comparison, CoP@NC was prepared utilizing the rod-like ZIF-67 as precursor. As shown in Fig. S20a, the rodlike ZIF-67 inclines to agglomerate, especially after pyrolysis at 600 ^{o}C under Ar and subsequent phosphorization (Fig. S20b-d). The HRTEM image shows that the distinct fringe spacings of 0.196 nm and 0.189 nm, which are assigned to (112) and (211) lattice planes of CoP, respectively (Fig. S20e). High-angle annular dark-field scanning transmission electron microscopy (HAADF-STEM) and energy-dispersive X-ray spectroscopy (EDS) elemental mapping images of CoP@NC indicate that C, N, P and Co are distributed evenly on the sample.

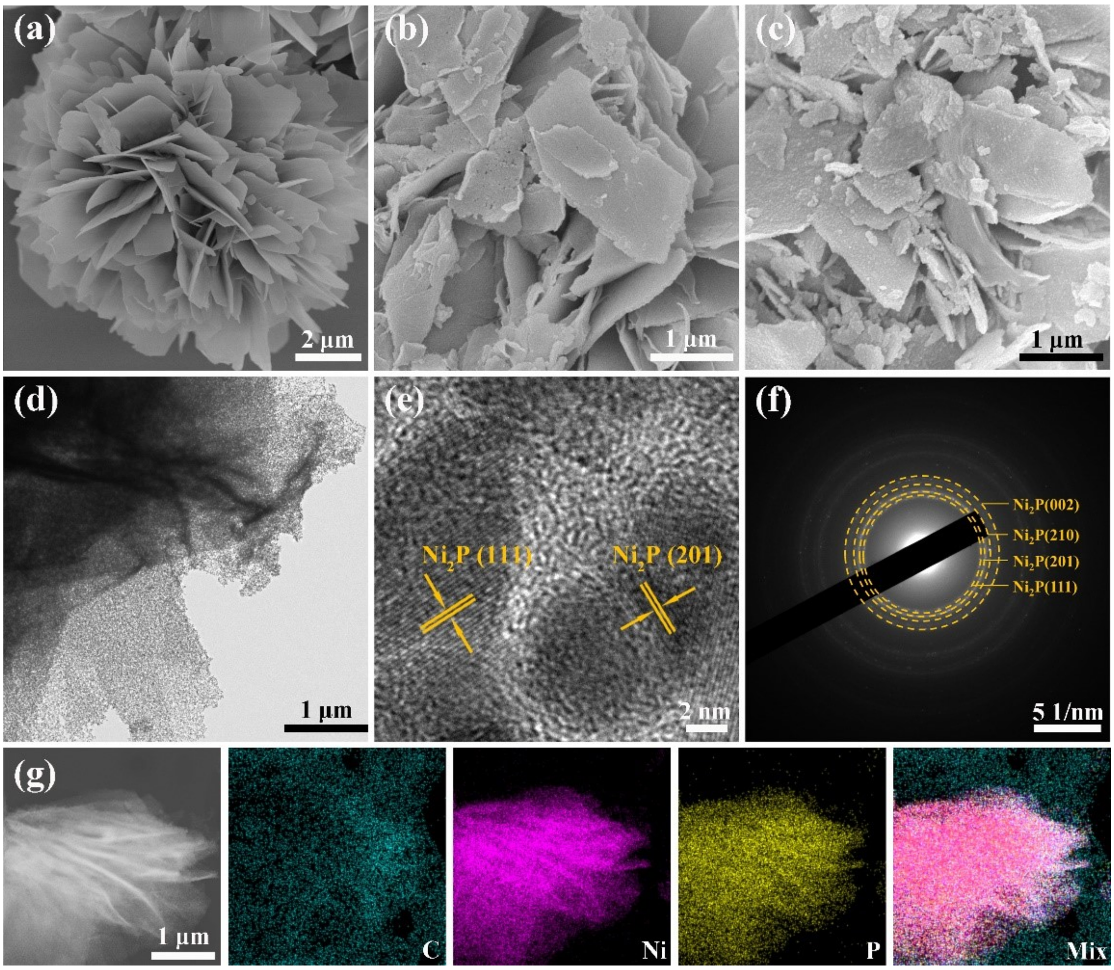

Fig. S21. SEM images of (a) Ni-BDC, (b) Ni@C, and (c) Ni_2P@C. (d) TEM image, (e) HRTEM image, (f) selected electron diffraction (SAED) image, and (g) HAADF-STEM and EDS mapping images of Ni_2P@C.

Fig. S21a-d shows that the petal-like nanosheets of Ni-BDC are inclined to agglomerate together or collapse during the calcination and phosphorization. HRTEM image shows the nanoparticles are encapsulated by carbon layers, exhibiting an interplanar spacing of 0.221 nm and 0.203 nm, in good agreement with the (111) and (201) planes of Ni_2P, respectively (Fig. S21e). Meanwhile, the main diffraction rings in the SAED image match with Ni_2P (Fig. S21f). Furthermore, HAADF-STEM and the related element mapping analysis exhibit that the elements of Ni, P, and C are uniformly distributed in the entire architecture (Fig. S21g).

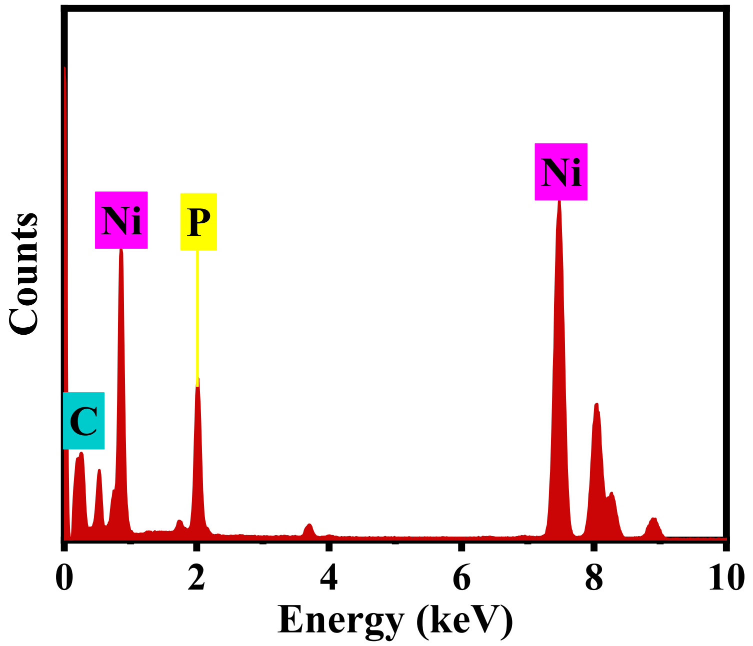

Fig. S22. Energy dispersive X-ray spectroscopy (EDS) spectrum of Ni_2P@C.

The energy dispersive X-ray spectroscopy (EDS) analysis also proves the presence of Ni, P, C and elements.

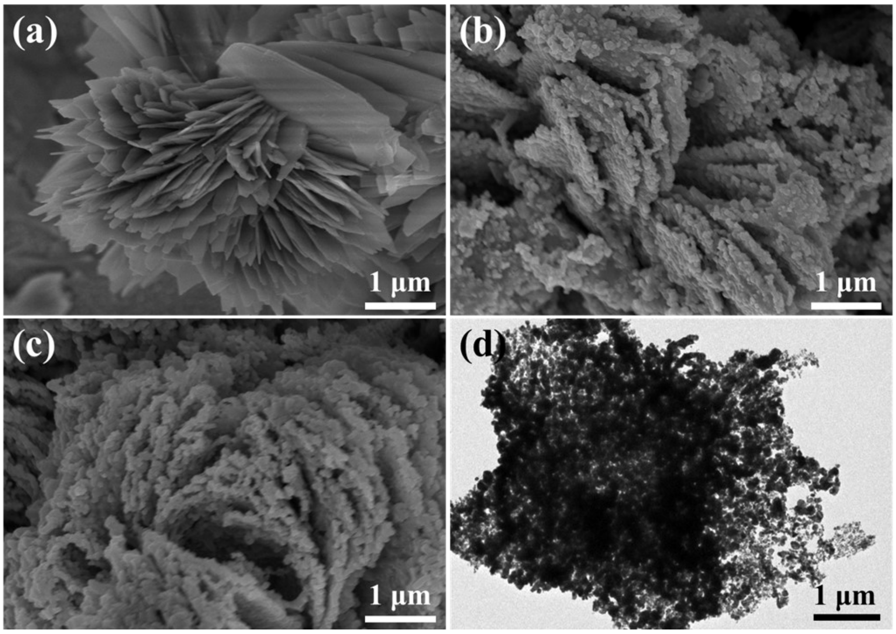

Fig. S23. SEM images of (a) NiCo-BDC, (b) Co-Ni-NiCo@C, (c) CoP-Ni_2P-NiCoP@C, and (d) TEM image of CoP-Ni_2P-NiCoP@C.

SEM images of NiCo-BDC show the nanosheet morphology is similar to Ni-BDC. After calcination and phosphorization, the nanosheets are incline to aggregate/stack.

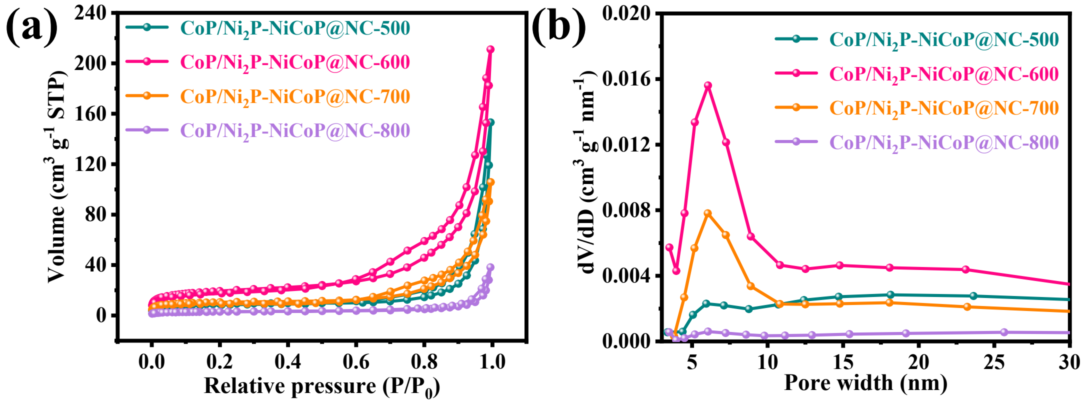

Fig. S24. (a) N_2 adsorption-desorption isotherms, and (b) the corresponding pore size distribution curves of CoP/Ni_2P-NiCoP@NC-T (T = 500, 600, 700 and 800 ^{o}C).

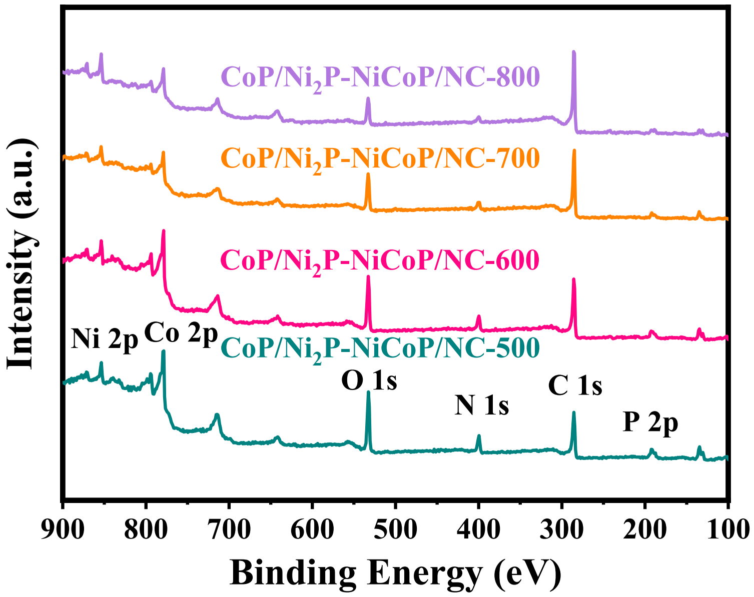

Fig. S25. XPS survey spectra of CoP/Ni_2P-NiCoP@NC-T (T = 500, 600, 700 and 800 °C).

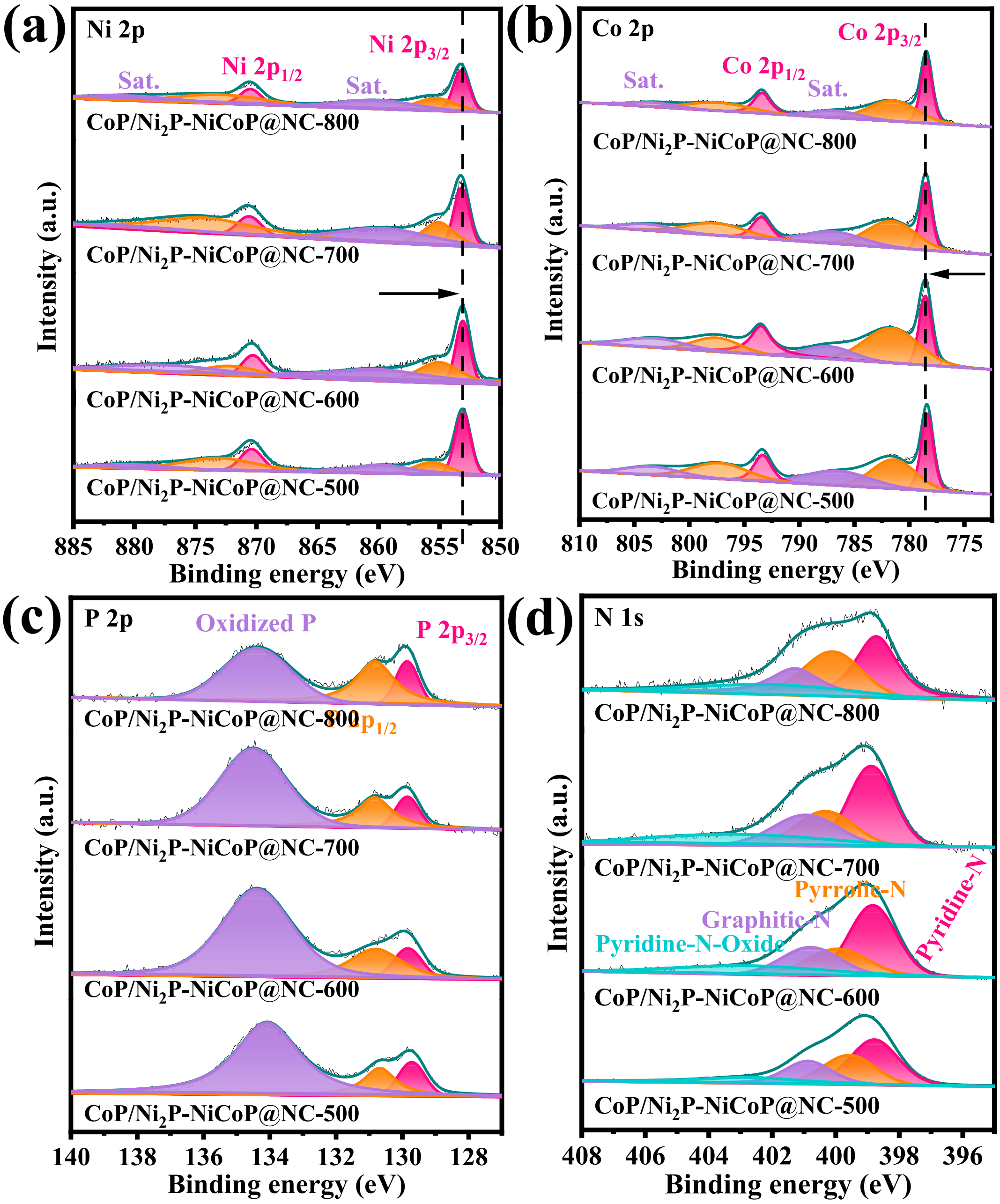

Fig. S26. XPS spectra of (a) Ni 2p, (b) Co 2p, (c) P 2p and (d) N 1s for CoP/Ni_2P-NiCoP@NC-T (T = 500, 600, 700 and 800 °C).

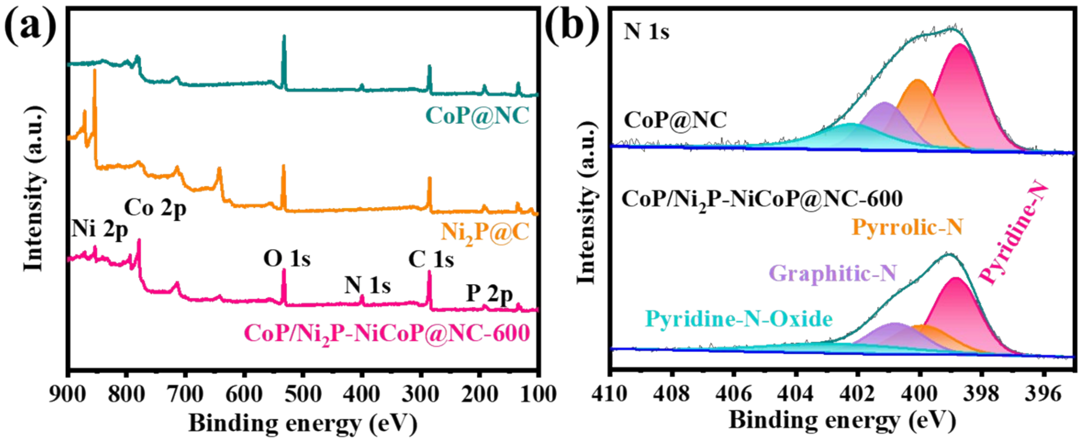

Fig. S27. (a) XPS survey spectra, (b) N 1s deconvoluted XPS spectra for CoP/Ni_2P-NiCoP@NC-600, Ni_2P@C and CoP@NC.

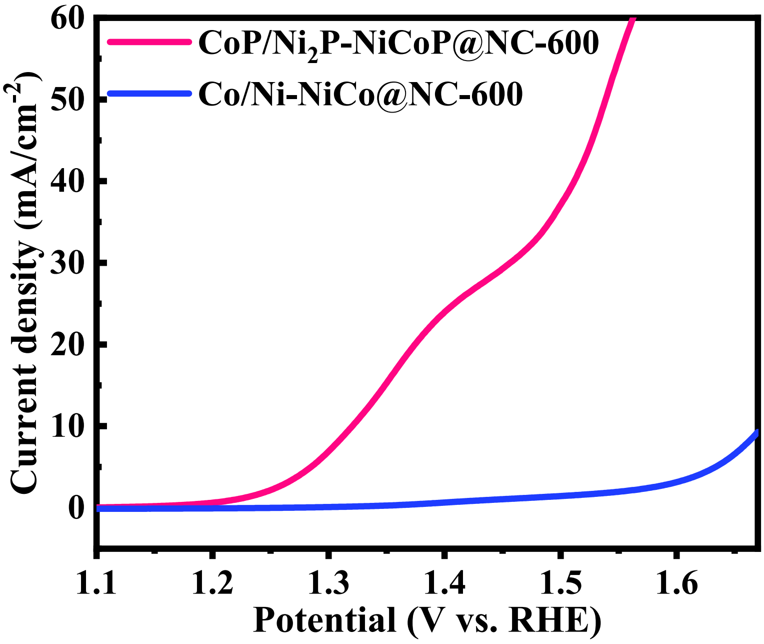

Fig. S28. Polarization curves of CoP/Ni$_2$P-NiCoP@NC-600 and Co/Ni-NiCo@NC-600 in 0.1 M KOH with 5 mM HMF.

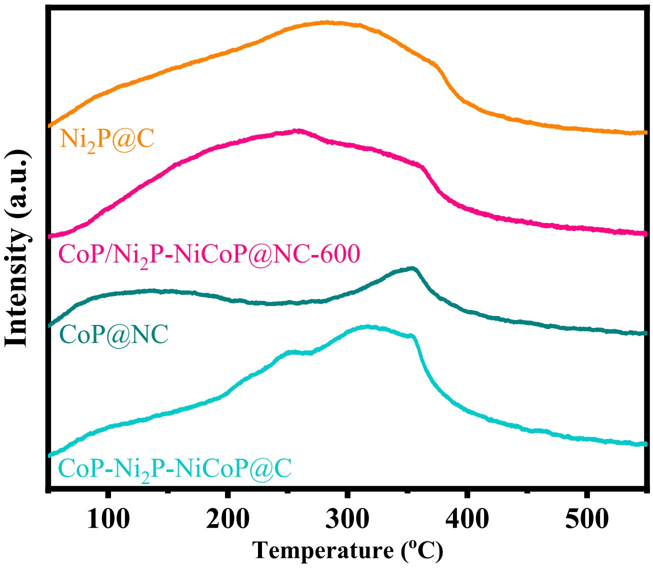

Fig. S29. H_2-TPD profiles of CoP/Ni$_2$P-NiCoP@NC-600, CoP@NC, Ni$_2$P@C and CoP-Ni$_2$P-NiCoP@C.

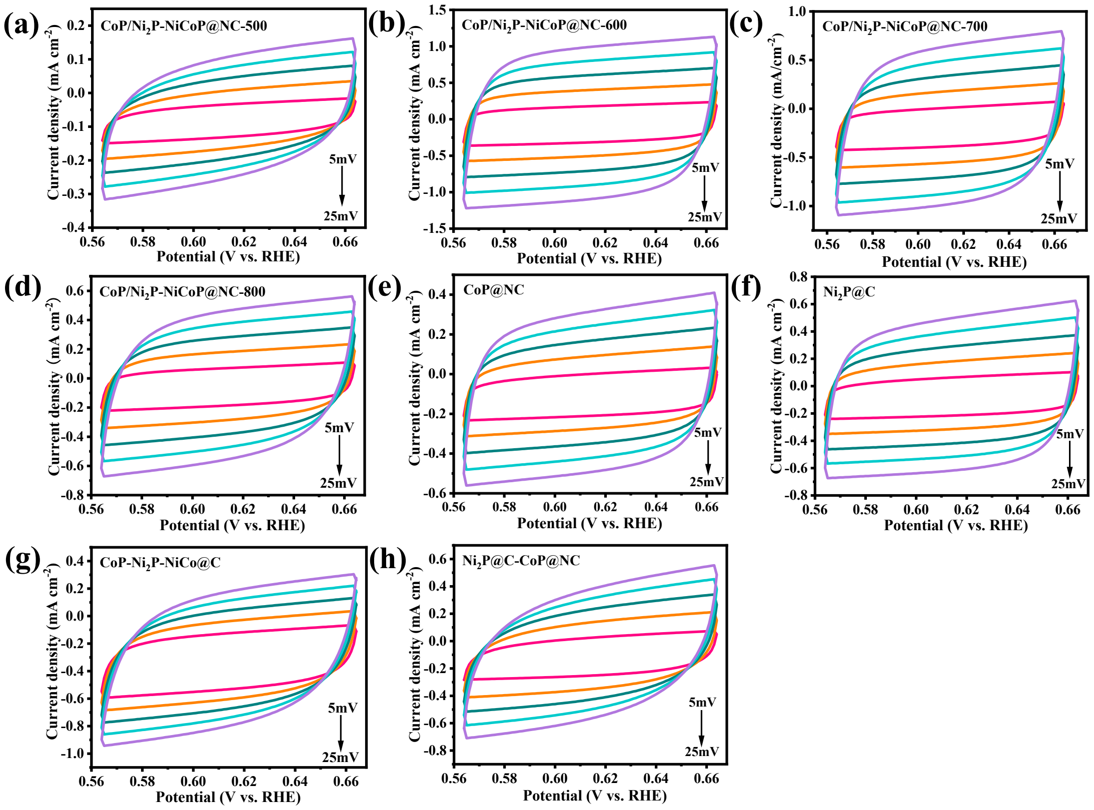

Fig. S30. CV curves of (a) CoP/Ni$_2$P-NiCoP@NC-500, (b) CoP/Ni$_2$P-NiCoP@NC-600, (c) CoP/Ni$_2$P-NiCoP@NC-700, (d) CoP/Ni$_2$P-NiCoP@NC-800, (e) CoP@NC, (f) Ni$_2$P@C, (g) CoP-Ni$_2$P-NiCoP@C and (h) Ni$_2$P@C-CoP@NC with HMF at different scan rates.

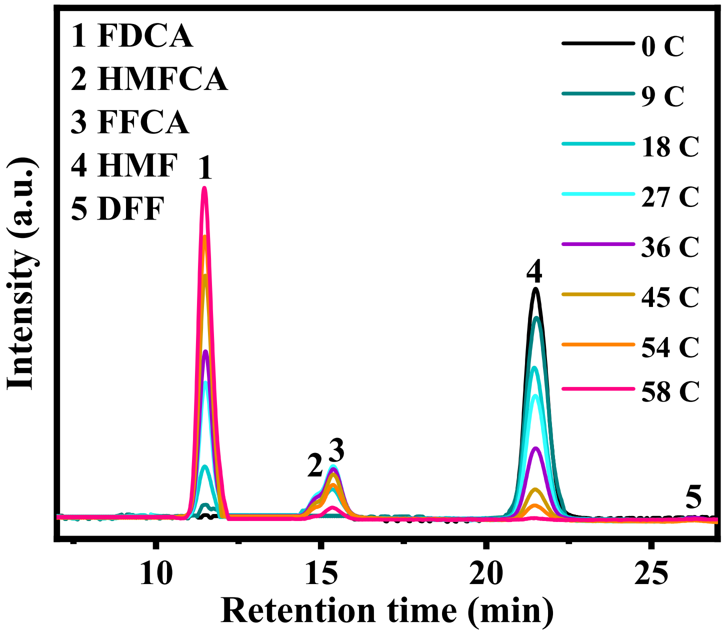

Fig. S31. HPLC traces of HMF electrooxidation catalyzed by CoP/Ni_2P-NiCoP@NC-600 at 1.45 V *vs.* RHE in 20 mL 0.1 M KOH with 5 mM HMF.

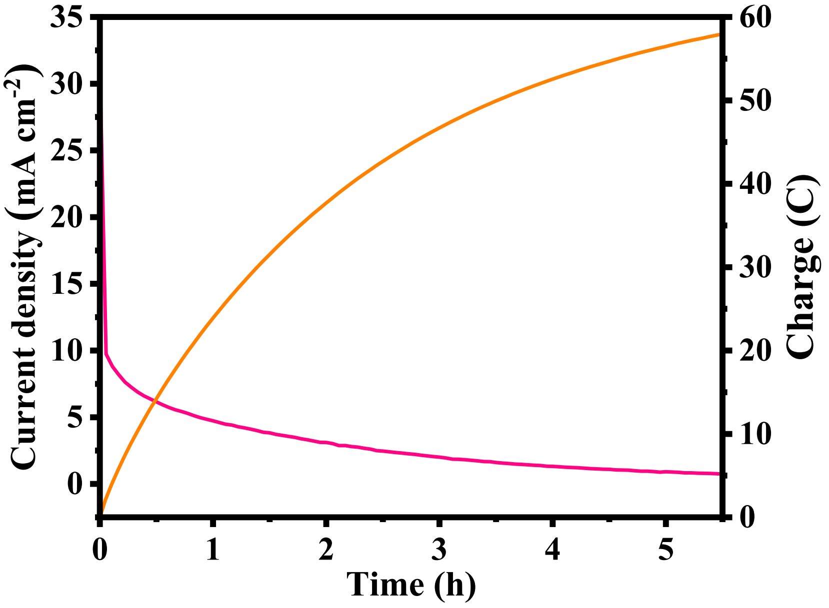

Fig. S32. I-t curve for CoP/Ni_2P-NiCoP@NC-600 at a constant potential of 1.45 V *vs.* RHE in 0.1 M KOH with 5 mM HMF by passing the charge of 58 C.

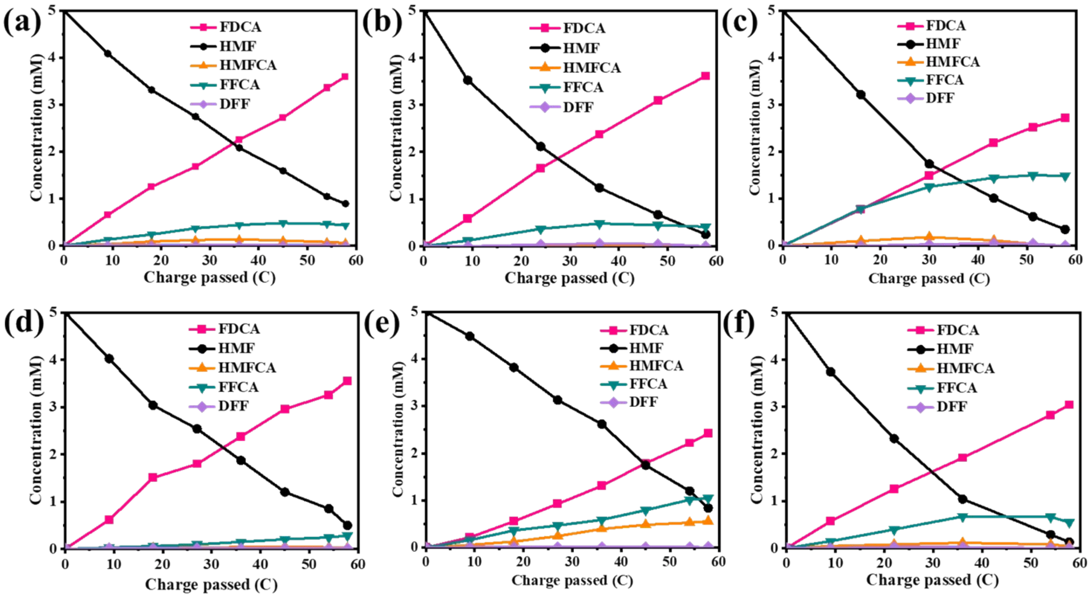

Fig. S33. Conversions of HMF during the electrooxidation for (a) CoP/Ni_2P-NiCoP@NC-500, (b) CoP/Ni_2P-NiCoP@NC-700, (c) CoP/Ni_2P-NiCoP@ NC-800, (d) Ni_2P@C, (e) CoP@NC and (f) Ni_2P@C-CoP@NC.

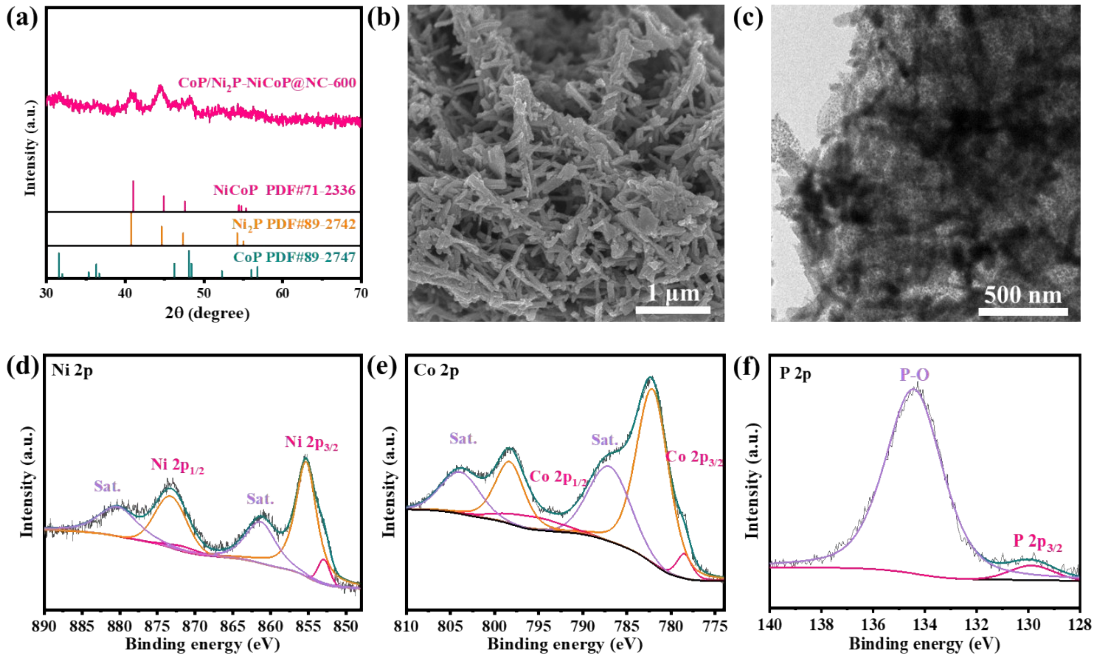

Fig. S34. (a) XRD patterns, (b) SEM image, (c) TEM image, XPS spectra of (d) Ni 2p, (e) Co 2p and (f) P 2p of CoP/Ni_2P-NiCoP@ NC-600 after HMF electrooxidation test.

Supplementary Tables

Table S1. BET surface areas and mesopore volumes of the samples.

Sample	S_{BET} (m^2 g^{-1})	Mesopore volume (cm^3 g^{-1})
NiCo-BDC@ZIF-67	218.0	0.184
Ni-BDC	23.0	0.106
CoP/Ni_2P-NiCoP@NC-500	31.1	0.234
CoP/Ni_2P-NiCoP@NC-600	**66.9**	**0.327**
CoP/Ni_2P-NiCoP@NC-700	35.6	0.164
CoP/Ni_2P-NiCoP@NC-800	10.1	0.057
Ni_2P@C	20.9	0.077
CoP@NC	13.5	0.043

Table S2. Element contents of the samples

Sample	Element content[a]		Relative content of the N species (%, based on XPS)				Element content[b]	
	C	N	Pyridinic N	Pyrrolic N	Graphic N	Pyridine -N- Oxide	Ni	Co
CoP/Ni_2P-NiCoP@NC-500	17.9	5.1	40.5	26.8	20.1	12.5	19.5	21.3
CoP/Ni_2P-NiCoP@NC-600	**23.0**	**4.3**	**42.1**	**20.1**	**20.7**	**17.0**	**22.9**	**23.7**
CoP/Ni_2P-NiCoP@NC-700	21.1	2.1	38.0	20.7	20.8	20.5	24.2	27.0
CoP/Ni_2P-NiCoP@NC-800	19.4	1.1	35.1	29.0	19.3	16.7	27.2	28.4
Ni_2P@C	12.2	-	-	-	-	-	61.1	-
CoP@NC	23.8	4.8	40.5	24.0	17.3	18.2	-	38.5

(a) The weight percentage of C and N were determined by elemental analysis.

(b) The weight percentage of Ni and Co were determined by Atomic Absorption Spectroscopy (AAS).

Table S3. Comparison of HMF electrooxidation reaction performances over different electrocatalysts in basic electrolyte.

Catalysts	pH	Oxidation potential (V *vs.* RHE)	FDCA yield (%)	FE (%)	Ref.
CoP/Ni_2P-NiCoP@NC-600	**13**	**1.32 (10)**	**98.1**	**97.6**	**This work**
NiCoBDC-NF	13	1.55 (10)	99	78.8	S10
Nanocrystalline Cu foam	13	1.62 (onset)	96.4	95	S11
$Ni(OH)_2/NiOOH$	13	1.47 (onset)	96.0	96	S12
$NiCo_2O_4$	13	1.37 (10)	90	100	S13
Ni(NS)/CP	13	1.36 (onset)	99.4	95.3	S14
$NiCo_2O_4$/NF	14	1.47 (10)	90.8	87.5	S15
NiCoFe-LDHs	14	1.52 (10)	95.5	84.9	S16
VN/NiF	14	1.36 (10)	96	86	S17
Co−P/CF	14	1.38 (10)	84	-	S18
$CuCo_2O_4$	14	1.40 (10)	93.7	94	S19
Ni_2P/NPA/NF	14	1.35 (onset)	97	97	S20
$CuNi(OH)_2$	14	1.45 (10)	93.3	93	S21
N-Ni_3S_2-MoO_2/NF	14	1.57 (50)	90	90	S22
Ni_3N	14	1.35 (50)	98	-	S23
Ni_3S_2/NF	14	1.47 (10)	-	100	S24
Co_3O_4	14	1.50 (10)	96.8	96.6	S25
Ir/Co_3O_4	14	1.38 (10)	98	98	S26
MoO_2-FeP@C	14	1.36 (10)	98.6	97.8	S27

Table S4. Number of surface Ni/Co atoms calculated from H_2-TPD analysis.

Sample	Number of surface Ni/Co (mol mg^{-1}) [a]
CoP/Ni_2P-NiCoP@NC-600	1.58×10^{-6}
Ni_2P@C	1.82×10^{-6}
CoP@NC	1.04×10^{-6}
CoP-Ni_2P-NiCoP@C	2.18×10^{-6}
Ni_2P@C-CoP@NC	1.35×10^{-6}

[a] Calculated from H_2-TPD analysis.

Table S5. Parameters for each catalyst investigated on carbon cloth electrode in 0.1 M KOH electrolyte with 5 mM HMF.

Sample	Geometric area (cm^2)	Potential (V *vs.* RHE)[a]	Mass activity[b] ($A\ g^{-1}$)[c]	TOF (h^{-1})[c]
CoP/Ni_2P-NiCoP@NC-600	1	1.32	35.3	116
Ni_2P@C	1	1.37	22.0	82
CoP@NC	1	1.46	15.6	64
CoP-Ni_2P-NiCoP@C	1	1.36	14.9	34
Ni_2P@C-CoP@NC	1	1.39	23.8	93

a: obtained at the current density of 10 $mA\cdot cm^{-2}$ (based on geometric area).

b: obtained at the potential of 1.45 V *vs.* RHE.

c: based on the surface Ni and Co atoms analyzed by H_2-TPD, calculated via equation (S5).

References

[S1]P. Giannozzi, S. Baroni, N. Bonini, M. Calandra, R. Car, C. Cavazzoni, D. Ceresoli, G. L. Chiarotti, M. Cococcioni, I. Dabo, A. Dal Corso, S. de Gironcoli, S. Fabris, G. Fratesi, R. Gebauer, U. Gerstmann, C. Gougoussis, A. Kokalj, M. Lazzeri, L. Martin-Samos, N. Marzari, F. Mauri, R. Mazzarello, S. Paolini, A. Pasquarello, L. Paulatto, C. Sbraccia, S. Scandolo, G. Sclauzero, A. P. Seitsonen, A. Smogunov, P. Umari and R. M. Wentzcovitch, *J. Phys.: Condens. Mat.*, 2009, **21**, 395502.

[S2]P. Giannozzi, O. Andreussi, T. Brumme, O. Bunau, M. Buongiorno Nardelli, M. Calandra, R. Car, C. Cavazzoni, D. Ceresoli, M. Cococcioni, N. Colonna, I. Carnimeo, A. Dal Corso, S. de Gironcoli, P. Delugas, R. A. DiStasio, A. Ferretti, A. Floris, G. Fratesi, G. Fugallo, R. Gebauer, U. Gerstmann, F. Giustino, T. Gorni, J. Jia, M. Kawamura, H. Y. Ko, A. Kokalj, E. Küçükbenli, M. Lazzeri, M. Marsili, N. Marzari, F. Mauri, N. L. Nguyen, H. V. Nguyen, A. Otero-de-la-Roza, L. Paulatto, S. Poncé, D. Rocca, R. Sabatini, B. Santra, M. Schlipf, A. P. Seitsonen, A. Smogunov, I. Timrov, T. Thonhauser, P. Umari, N. Vast, X. Wu and S. Baroni, *J. Phys.: Condens. Mat.*, 2017, **29**, 465901.

[S3]P. Giannozzi, O. Baseggio, P. Bonfà, D. Brunato, R. Car, I. Carnimeo, C. Cavazzoni, S. d. Gironcoli, P. Delugas, F. F. Ruffino, A. Ferretti, N. Marzari, I. Timrov, A. Urru and S. Baroni, *J. Chem. Phys.*, 2020, **152**, 154105.

[S4]J. P. Perdew, K. Burke and M. Ernzerhof, *Phys. Rev. Lett.*, 1996, **77**, 3865-3868.

[S5]P. E. Blöchl, O. Jepsen and O. K. Andersen, *Phys. Rev. B*, 1994, **49**, 16223-16233.

[S6]G. Kresse and D. Joubert, *Phys. Rev. B*, 1999, **59**, 1758-1775.

[S7]H. J. Monkhorst and J. D. Pack, *Phys. Rev. B*, 1976, **13**, 5188-5192.

[S8]D. W. Lee, L. De Los Santos V, J. W. Seo, L. Leon Felix, A. Bustamante D, J. M. Cole and C. H. W. Barnes, *J. Phys. Chem. B*, 2010, **114**, 5723-5728.

[S9]L. Chai, Z. Hu, X. Wang, Y. Xu, L. Zhang, T.-T. Li, Y. Hu, J. Qian and S. Huang, *Adv. Sci.*, 2020, **7**, 1903195.

[S10] M. Cai, Y. Zhang, Y. Zhao, Q. Liu, Y. Li and G. Li, *J. Mater. Chem. A*, 2020, **8**, 20386-20392.

[S11] D.-H. Nam, B. J. Taitt and K.-S. Choi, *ACS Catal.*, 2018, **8**, 1197-1206.

[S12] B. J. Taitt, D.-H. Nam and K.-S. Choi, *ACS Catal.*, 2019, **9**, 660-670.

[S13] L. Gao, Y. Bao, S. Gan, Z. Sun, Z. Song, D. Han, F. Li and L. Niu, *ChemSusChem*, 2018, **11**, 2547-2553.

[S14] X. Lu, K.-H. Wu, B. Zhang, J. Chen, F. Li, B.-J. Su, P. Yan, J.-M. Chen and W. Qi, *Angew. Chem. Int. Ed.*, 2021, **60**, 14528-14535.

[S15] M. J. Kang, H. Park, J. Jegal, S. Y. Hwang, Y. S. Kang and H. G. Cha, *Appl. Catal. B: Environ.* 2019, **242**, 85-91.

[S16] M. Zhang, Y. Liu, B. Liu, Z. Chen, H. Xu and K. Yan, *ACS Catal.*, 2020, **10**, 5179-5189.

[S17] S. Li, X. Sun, Z. Yao, X. Zhong, Y. Cao, Y. Liang, Z. Wei, S. Deng, G. Zhuang, X. Li and J. Wang, *Adv. Funct. Mater.*, 2019, **29**, 1904780.

[S18] N. Jiang, B. You, R. Boonstra, I. M. Terrero Rodriguez and Y. Sun, *ACS Energy Lett.*, 2016, **1**, 386-390.

[S19] Y. Lu, C.-L. Dong, Y.-C. Huang, Y. Zou, Z. Liu, Y. Liu, Y. Li, N. He, J. Shi and S. Wang, *Angew. Chem. Int. Ed.*, 2020, **59**, 19215-19221.

[S20] B. You, N. Jiang, X. Liu and Y. Sun, *Angew. Chem. Int. Ed.*, 2016, **55**, 9913-9917.

[S21] H. Chen, J. Wang, Y. Yao, Z. Zhang, Z. Yang, J. Li, K. Chen, X. Lu, P. Ouyang and J. Fu, *ChemElectroChem*, 2019, **6**, 5797-5801.

[S22] L. Wang, J. Cao, C. Lei, Q. Dai, B. Yang, Z. Li, X. Zhang, C. Yuan, L. Lei and Y. Hou, *ACS Appl. Mater. Inter.*, 2019, **11**, 27743-27750.

[S23] N. Zhang, Y. Zou, L. Tao, W. Chen, L. Zhou, Z. Liu, B. Zhou, G. Huang, H. Lin and S. Wang, *Angew. Chem. Int. Ed.*, 2019, **58**, 15895-15903.

[S24] B. You, X. Liu, N. Jiang and Y. Sun, *J. Am. Chem. Soc.*, 2016, **138**, 13639-13646.

[S25] Z. Zhou, C. Chen, M. Gao, B. Xia and J. Zhang, *Green Chem.*, 2019, **21**, 6699-6706.

[S26] Y. Lu, T. Liu, C.-L. Dong, Y.-C. Huang, Y. Li, J. Chen, Y. Zou and S. Wang, *Adv. Mater.*, 2021, **33**, 2007056.

[S27] G. Yang, Y. Jiao, H. Yan, Y. Xie, A. Wu, X. Dong, D. Guo, C. Tian and H. Fu, *Adv. Mater.*, 2020, **32**, 2000455